LES OF JET FROM TRUNCATED IDEALLY CONTOURED NOZZLES IN OVER-EXPANDED CONDITIONS

Ilyan Pingault[2], **Romain Gojon**[1,*], **Stéphane Jamme**[1], **Jérémie Gressier**[1], **Vincent Jaunet**[2], **Guillaume Lehnasch**[2]
[1]ISAE-SUPAERO, Université de Toulouse, France
[2]ISAE-ENSMA, PPRIME, France
*email: romain.gojon@isae-supaero.fr

ABSTRACT

The performance of supersonic nozzles employed in space propulsion is primarily governed by the delivery of maximum thrust at high altitudes. This design choice implies that during engine start-up at low altitudes, the nozzle operates in an over-expanded regime. Under such conditions, pressure mismatch at the nozzle exit induces an adverse pressure gradient, which leads to jet column contraction, the formation of recompression shocks, and internal flow separation. These phenomena generate non-axisymmetric and unsteady wall-pressure fluctuations, which can lead to severe side-loads that can compromise the structural integrity of the nozzle. Therefore, reliable prediction of side-loads characteristics constitutes a critical challenge to improve both the performance and the safety of space launch systems. However, a predictive modeling framework for side-loads generation is still lacking. To address this, wall-modeled Large Eddy Simulations are performed as a high-fidelity numerical model, allowing a more in-depth analysis of the unsteady characteristics of the flow leading to these lateral loads.

INTRODUCTION

As shown by Dumnov (1996), the computation of the off-axis forces spectra acting on the nozzle wall requires the knowledge of the cross-spectral density (CSD) of the first azimuthal Fourier mode of wall pressure. This means that the wall pressure field inside the nozzle must be resolved both spatially and temporally. This is still a challenge both experimentally, where the limited optical access inside the nozzle prohibits the acquisition of the entire pressure field, and numerically, due to the necessary computing and storing resources required.

The Delayed Detached Eddy Simulation (DDES) turned out to be relatively effective in capturing the main trends of the unsteady pressure field for different nozzle geometries and flow conditions (see Deck (2009), Shams *et al.* (2013) and Martelli *et al.* (2020), for example). However, this modeling approach requires careful mesh adjustments and corrections to the underlying Reynolds Averaged Navier-Stokes (RANS) model on which it is built. Standard second-order finite volume schemes limit the ability to faithfully capture the full flow dynamics. A major difficulty also lies in the need to store all the unsteady data (both wall pressure signals and unsteady flow field) within large computational zones over a rather long time, to extract the large coherent turbulent structures responsible for the low-frequency wall pressure signature. For the particular Truncated Ideally Contoured (TIC) nozzle geometry considered here, this was recently made possible only at an interesting resonant frequency in Bakulu *et al.* (2021), focusing on the extraction of associated coherent structures and omitting the rest of the spectra.

This study aims to further these efforts towards a better understanding of over-expanded flow dynamics via the use of Wall-Modeled Large Eddy Simulations (WMLES). Access to the entire flow field may provide insights on the coherent structures dominating the flow field and those responsible for wall pressure fluctuations and, therefore, side-loads.

NUMERICAL SETUP
Operating points

The TIC nozzle considered in this work was designed with the method of characteristics for a design Mach number of $M_d = 3.5$. The divergent section has a length of $L = 0.183$m, and the throat diameter is $D_t = 0.038$m. More information on this nozzle can be found in Jaunet *et al.* (2017) and in Bakulu *et al.* (2021). In the present study, we focus on a Nozzle Pressure Ratio (NPR) of 9 in order to reproduce the resonant mechanism previously observed.

Numerical methods

WMLES is carried out with the massively parallel in-house solver IC^3 (Bergier *et al.* (2023); Vittal-Shenoy *et al.* (2023)). The code solves the filtered compressible Navier–Stokes equations in conservative form using a finite-volume formulation on unstructured grids. Spatial fluxes are evaluated with a hybrid discretization scheme that combines a fourth-order central method and a third-order upwind method, where the blending parameter is determined by the local mesh quality or triggered by specific sensors. Time advancement is performed using an explicit third-order Runge–Kutta scheme. The subgrid-scale dynamics is modeled using the approach proposed by Vreman (2004).

Fig. 1 shows a schematic of the computational grid near the nozzle. The computational domain contains 122 blocks of structured grids and consists of 430 million hexahedral elements. The total size of the computational domain is $-8D_t < x < 50D_t$ in the streamwise direction and $0 < r < 13D_t$ in the radial direction. In the azimuthal direction, $n_\theta = 800$ points are used. Inside the nozzle, in the wall-normal direction, the grid is gradually refined near the surface to reach a first cell having a wall-normal dimension of $\Delta n = 1.5 \times 10^{-6}$m, which allows us to locally reach $\Delta n^+ = u_\tau \Delta n / \nu = 70$, where u_τ is the friction velocity and ν the kinematic viscosity. This value

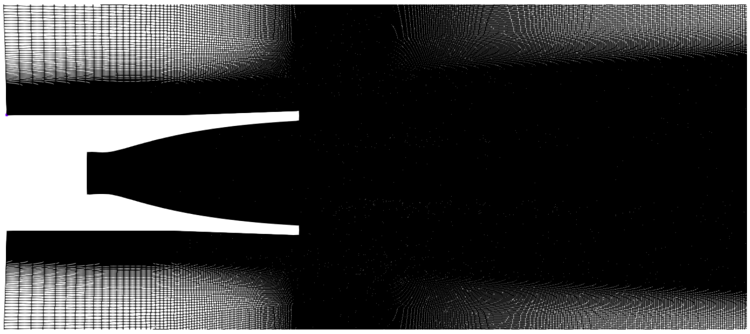

Figure 1. Radial cut of the mesh around the nozzle geometry.

falls within the appropriate range for the wall model used in this work. The one implemented in the IC^3 solver uses 1D RANS equilibrium boundary layer equations on a normal line, embedded in the LES grid (Bodart & Larsson (2011); Bodart *et al.* (2013)). At a certain height, here $h_{wm} = 0.3$ mm, the wall model takes information from the LES and then computes the wall shear stress τ_w. This latter value is given back to the LES as a boundary condition at the wall. The mesh is coarsened in a sponge zone used when progressing toward the outlet and the far-field region, to dampen acoustic waves and hydrodynamic fluctuations before they reach the boundaries. The digital filtering technique (Touber & Sandham (2009)) is applied at the inlet to spatially develop a fully turbulent boundary layer on the nozzle side walls. In this approach, zero-mean, unit-variance perturbations are imposed on mean flow quantities, following Reynolds-stress profiles imposed at the inlet. The perturbations are spatially modulated with the turbulence integral length scales in each direction (see Klein *et al.* (2003) and Xie & Castro (2008) for further details). In this work, data from turbulent boundary layer DNS results by Jiménez *et al.* (2010) were used for a $Re_\theta = 1960$. These data were rescaled to match the operating conditions at the inlet, assuming a boundary layer thickness that corresponds to 5% of the throat diameter. Turbulent length scales are taken equal to 2mm in the axial direction and 0.5mm in the radial and azimuthal directions.

RESULTS

In this section, LES results obtained for NPR=9 are examined. The inner nozzle wall was sampled at a frequency of $150kHz$ over 9501 snapshots and the jet flowfield was saved on a plane crossing the nozzle axis. First, a snapshot of the flowfield is given in Fig. 2. For this case, as expected in over-expanded conditions, the flow detaches from the nozzle in the diverging part. This separation leads to the formation of compression shocks that later downstream produce a shock cell structure similar to the one observed in classical non-ideally expanded supersonic jets. In the near acoustic field, similar to a conventional non-ideally expanded supersonic jet, it is observed that low-frequency mixing noise propagates in the downstream direction, while higher-frequency mixing noise propagates radially. Low-frequency waves are also visible in the upstream direction. The latter could be linked to a resonance mechanism appearing in the jet, similar to the screech noise mechanism.

Before considering the mean flow, the convergence of the wall pressure statistical quantities is first assessed. To this end, on Fig. 3 and Fig. 4, the local evolution of the statistics is examined as function of the samples k used for averaging. In the separated region, both the mean and rms exhibit rapid convergence, reaching within 1% and 2.5% of their final values, respectively. However, in the vicinity of the separation region, the convergence appears to be slower, reflecting the low-frequency dynamics dominance at that location. The resulting mean flow is presented in Fig. 5 and 6.

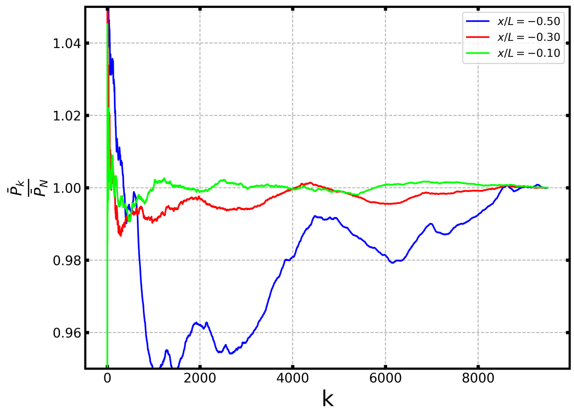

Figure 3. Mean wall pressure convergence.

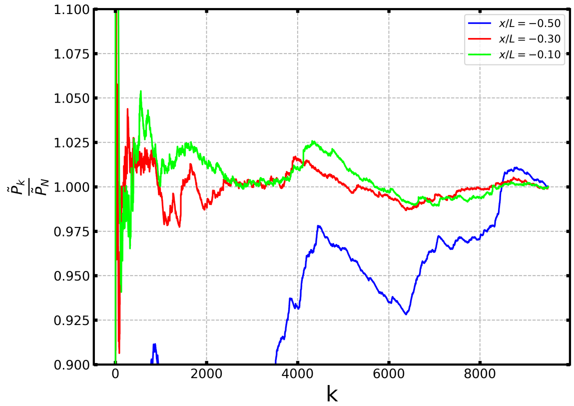

Figure 4. Wall pressure rms convergence.

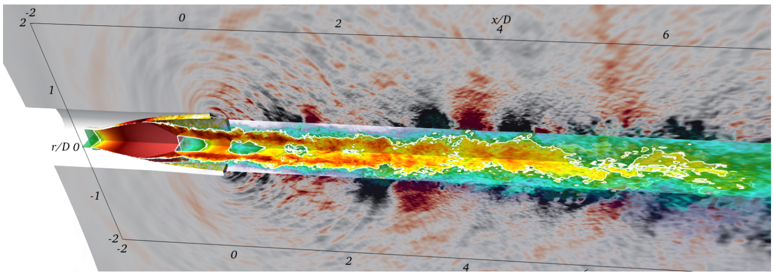

Figure 2. Radial slices of fluctuating density along two perpendicular planes near the jet axis and overall view of fluctuating pressure outside of the jet for NPR9.

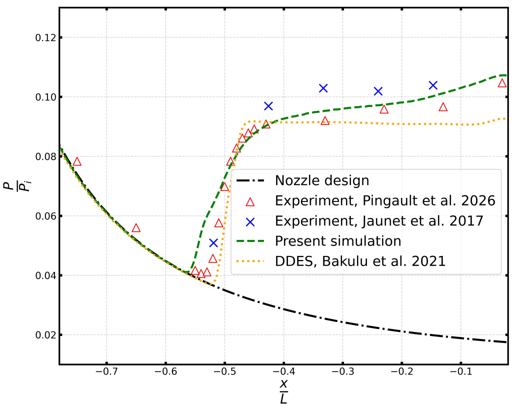

Figure 5. Mean pressure at the nozzle wall. The pressure is scaled by the total pressure P_i and the axial position by the nozzle divergent length L. The mean pressure profile results from averaging both in time and in the azimuthal direction.

The mean flow on the nozzle wall is found to exhibit a slight non-axisymmetry. To assess the degree of asymmetry of the mean flow, axial mean and root-mean-square (rms) pressure profiles at fixed azimuthal position are compared to the azimuthally-averaged mean and rms axial profiles using a normalized dot product denoted β. An overall β value close to unity denotes a high degree of axisymmetry, the minimum value computed for the mean wall pressure is 0.9997, while a value of 0.997 is found for the rms pressure, indicating an overall satisfactory level of axisymmetry. The steady side-loads associated with this non-axisymmetry are estimated by integration of the mean wall pressure distribution and represent only 2% of the thrust produced by the diverging section at NPR=9.

The mean flow is compared with data obtained at the S150 blow-down wind tunnel of Pprime institute in Poitiers (see Pingault *et al.* (2026) for more details). The pressure evolution along the nozzle axis obtained herein is compared with experimental and numerical data in Fig. 5. In spite of the non-axisymmetry found earlier, we can see a good overall agreement between the datasets. Although the present LES shows a jet detaching slightly upstream of the position measured experimentally, the internal triple point and Mach disk locations seem to be properly captured, as well as the subsequent structure of the jet downstream of the nozzle exit. As shown in Fig .6, the associated average velocity field appears to be in good agreement with experimental Particle Image Velocimetry (PIV) measurements.

The unsteady dynamics are now described. The data are temporally filtered by a Butterworth low-pass filter with a cut-off frequency of $10kHz$, enabling a more relevant comparison with experimental results as recommended in Martelli *et al.* (2020). The unsteady side-loads are computed by direct integration of the pressure on the nozzle wall. In Fig. 7, the resulting Power Spectral Density (PSD) is compared with the PSD obtained by integration of the CSD of the first azimuthal pressure mode $S_{pp,1,\omega}$ according to Dumnov (1996):

$$F_\omega = 4\pi^2 \int_0^L \int_0^L r(z)r(x)S_{pp,1,\omega}(x,z)dxdz, \qquad (1)$$

where r denotes the nozzle radius and L is the length of the diverging section.

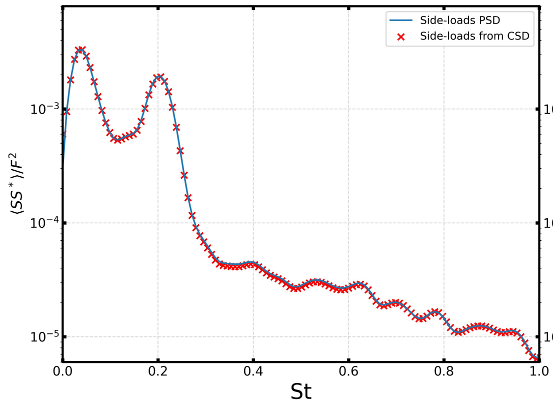

Figure 7. Estimated aerodynamic side-loads spectrum.

The PSD based on CSD of first azimuthal mode only is in perfect agreement with the PSD computed by direct integration of unsteady forces. This is an interesting practical validation of the expected theoretical fact that only the first azimuthal mode contributes to side-loads. The second peak is related to a screech-like resonance (Jaunet *et al.* (2017); Bakulu *et al.* (2021)). The PSD of the wall pressure fluctuations is computed at each position in the nozzle and averaged in the azimuthal direction. The resulting PSD map is shown in Figure. 8. It is clear that wall pressure is dominated by low frequencies in the vicinity of the separation shock (*i.e.* $-0.6 < x/L < -0.45$). A high amplitude band is also visible around $St = 0.2$ in the whole separated region corresponding to the peak previously observed in the PSD of side-loads.

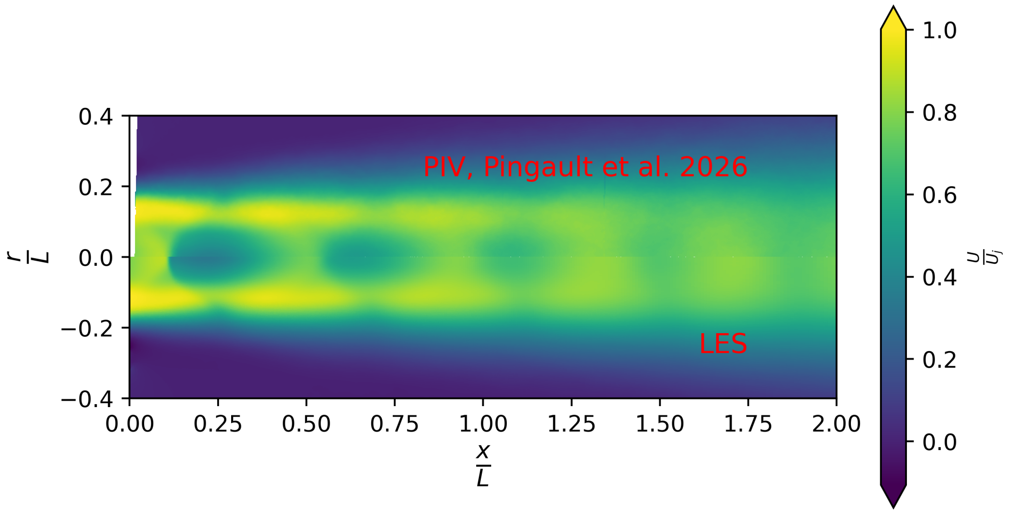

Figure 6. Mean streamwise velocity in the jet. The upper part of the figure shows the mean streamwise velocity measured by PIV and the lower part shows the mean streamwise velocity of the present simulation. The distances are scaled by the divergent length L and the velocity is scaled by the fully expanded jet velocity U_j.

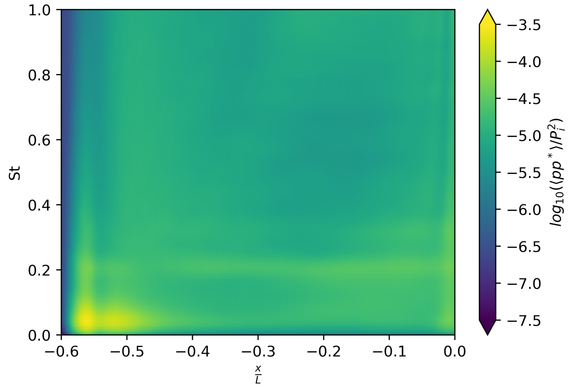

Figure 8. PSD map of the wall pressure fluctuations. The PSD is scaled by the total pressure P_i and plotted on a base-10 logarithmic scale.

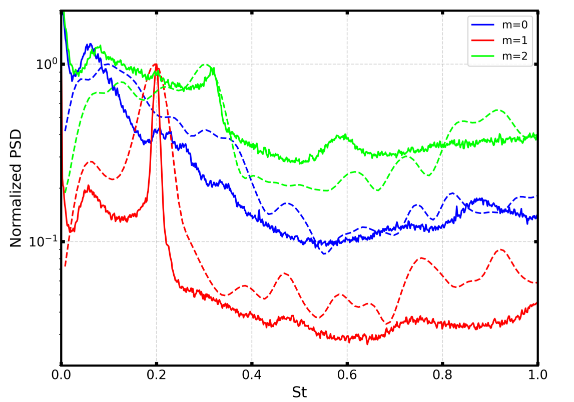

Figure 9. Spectra of the three first azimuthal Fourier modes at $\frac{x}{L} = -0.15$. The solid lines denote the experimental data from Jaunet *et al.* (2017) while dashed lines represent the LES data. The spectra are normalized by the maximum value found on the interval $0.1 < St < 1$.

Wall-pressure fluctuations are decomposed into azimuthal Fourier modes at a streamwise location $\frac{x}{L} = -0.15$ and shown in Fig. 9. It is clear from this figure that the dynamics at $St = 0.2$ is dominated by the first azimuthal non-axisymmetric Fourier mode. This dynamics was already reported in both numerical and experimental studies (see Tarsia Morisco *et al.* (2023), Jaunet *et al.* (2017), Martelli *et al.* (2020) or Bakulu *et al.* (2021) for further details).

To identify the coherent structures existing within the flow, a SPOD (Towne *et al.* (2018)) is conducted on the wall pressure fluctuations. The data is split into blocks of 512 time steps each with an overlap of 50%. The resulting SPOD spectrum shown in Fig. 10 displays a low rank dynamic with the two first modes dominating at $St = 0.2$, as it could have been anticipated from the previous results. The leading SPOD mode at $St = 0.2$ is represented in Fig. 11. It clearly shows an antisymmetric structure along the azimuthal direction, as expected for a side-load generating structure. An interesting feature is the phase shift between the shock interaction region (*i.e.* $-0.6 < x/L < -0.45$) and the separated one (*i.e.* $-0.45 < x/L$). This was already observed in Bakulu *et al.* (2021) and theoretically explained for a normal shock in Hurrell (1957); Culick & Rogers (1983).

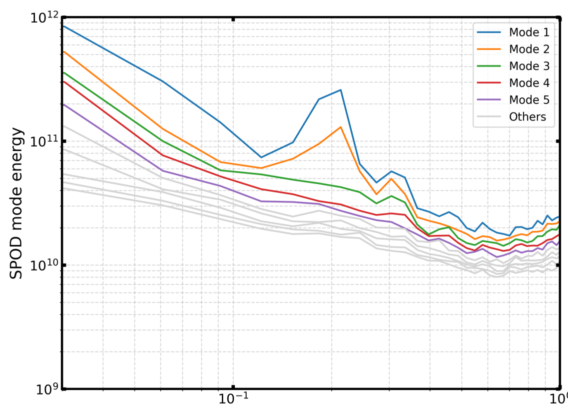

Figure 10. SPOD Spectrum.

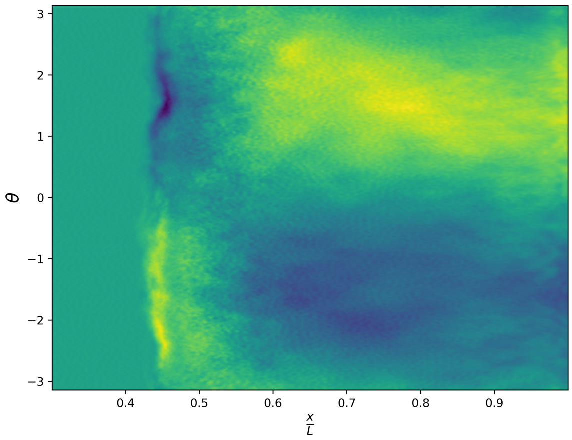

Figure 11. Leading SPOD mode at St=0.2.

CONCLUSION

A LES was performed on a TIC nozzle operating in overexpanded regime. The results obtained at NPR=9 were validated against experimental data and the convergence of the statistical quantities was checked. The unsteady behavior of wall pressure flow was investigated, and the mechanisms responsible for side-loads were observed, demonstrating the ability of the present computational strategy to elude the complex coherent structures that are associated to the generation of side-loads. Future work will focus on a more detailed analysis of the coherent structures driving the flow dynamics at $St = 0.2$ through the reconstruction of the helical mode in the jet. These data provide valuable insights for the development of side-loads prediction models.

REFERENCES

Bakulu, F., Lehnasch, G., Jaunet, V., da Silva, Eric G. & Girard, S. 2021 Jet resonance in truncated ideally contoured nozzles. *Journal of Fluid Mechanics* **919**, A32.

Bergier, T., Gojon, R., Fiore, M., Gressier, J., Jamme, S. & Joly, L. 2023 Sweep effects on a canonical shock wave/boundary layer interaction. *International Journal of Heat and Fluid Flow* **104**, 109227.

Bodart, J. & Larsson, J. 2011 Wall-modeled large eddy simulation in complex geometries with application to high-lift devices. In *CTR Annual Research Briefs*, pp. 37–48.

Bodart, J., Larsson, J. & Moin, P. 2013 Large eddy simulation of high-lift devices. In *21st AIAA Computational Fluid Dynamics Conference*, p. 2724.

Culick, F.E.C. & Rogers, T. 1983 The response of normal shocks in diffusers. *AIAA Journal* **21** (10), 1382–1390.

Deck, Sébastien 2009 Delayed detached eddy simulation of the end-effect regime and side-loads in an overexpanded nozzle flow. *Shock waves* **19** (3), 239–249.

Dumnov, G. 1996 Unsteady side-loads acting on the nozzle with developed separation zone. *32nd AIAA/ASME/SAE/ASEE Joint Propulsion Conference and Exhibit* pp. 1–8.

Hurrell, Herbert G 1957 Analysis of shock motion in ducts during disturbances in downstream pressure. *Tech. Rep.*.

Jaunet, V., Arbos, S., Lehnasch, G. & Girard, S. 2017 Wall pressure and external velocity field relation in overexpanded supersonic jets. *AIAA Journal* **55** (12), 4245–4257.

Jiménez, J., Hoyas, S., Simens, M.P. & Mizuno, Y. 2010 Turbulent boundary layers and channels at moderate reynolds numbers. *Journal of Fluid Mechanics* **657**, 335–360.

Klein, M., Sadiki, A. & Janicka, J. 2003 A digital filter based generation of inflow data for spatially developing direct numerical or large eddy simulations. *Journal of Computational Physics* **186** (2), 652–665.

Martelli, E., Saccoccio, L., Ciottoli, P. P., Tinney, C. E., Baars, W. J. & Bernardini, M. 2020 Flow dynamics and wall-pressure signatures in a high-reynolds-number overexpanded nozzle with free shock separation. *Journal of Fluid Mechanics* **895**, A29.

Pingault, I., Eysseric, D., Moreau, E., Girard, S., Lehnasch, G. & Jaunet, V. 2026 Detailed characterization of unsteady dynamics of highly separated jets in a truncated ideally contoured nozzle. In *60th 3AF International Conference on Applied Aerodynamics*.

Shams, A, Lehnasch, G, Comte, P, Deniau, H & de Roquefort, T Alziary 2013 Unsteadiness in shock-induced separated flow with subsequent reattachment of supersonic annular jet. *Computers & Fluids* **78**, 63–74.

Tarsia Morisco, Cosimo, Robinet, Jean-Christophe, Herpe, Julien & Saucereau, Didier 2023 Impinging shear layer instability in over-expanded nozzle dynamics. *Physics of Fluids* **35** (11), 116118 (1–17).

Touber, E. & Sandham, N. D. 2009 Large-eddy simulation of low-frequency unsteadiness in a turbulent shock-induced separation bubble. *Theoretical and Computational Fluid Dynamics* **23**, 79–107.

Towne, A., Schmidt, O. T. & Colonius, T. 2018 Spectral proper orthogonal decomposition and its relationship to dynamic mode decomposition and resolvent analysis. *Journal of Fluid Mechanics* **847**, 821–867.

Vittal-Shenoy, D., Gojon, R., Jardin, T. & Jacob, M. C. 2023 Angle-of-attack and Mach number effects on the aeroacoustics of an SD7003 airfoil at Reynolds number 60,000. *International Journal of Aeroacoustics* **22** (1-2), 131–152.

Vreman, A. W. 2004 An eddy-viscosity subgrid-scale model for turbulent shear flow: Algebraic theory and applications. *Physics of Fluids* **16** (10), 3670–3681.

Xie, Z.-T. & Castro, I. P. 2008 Efficient generation of inflow conditions for large eddy simulation of street-scale flows. *Flow, Turbulence and Combustion* **81**, 449–470.